RSC Advances

ROYAL SOCIETY OF CHEMISTRY

www.rsc.org/advances

RSC advances

Dynamic Article Links ►

Cite this: DOI: 10.1039/c0xx00000x

www.rsc.org/xxxxxx

PAPER

Influence of crystal structure on the electrochemical performance of A-site-deficient $Sr_{1-s}Nb_{0.1}Co_{0.9}O_{3-\delta}$ perovskite cathodes

Yinlong Zhu,[a] Ye Lin,[b] Xuan Shen,[c,d] Jaka Sunarso,[e] Wei Zhou,[*,f] Shanshan Jiang,[a] Dong Su,[c] Fanglin Chen,[b] and Zongping Shao[*,g]

Received (in XXX, XXX) Xth XXXXXXXXX 20XX, Accepted Xth XXXXXXXXX 20XX

DOI: 10.1039/b000000x

The creation of A-site cation defects within perovskite oxides can alter substantially the structure and properties of its stoichiometric analogue. In this work, we demonstrate that by vacating 2 and 5% of A-site cation from $SrNb_{0.1}Co_{0.9}O_{3-\delta}$ (SNC1.00) perovskites ($Sr_{1-s}Nb_{0.1}Co_{0.9}O_{3-\delta}$, s = 0.02 and 0.05; denoted as SNC0.98 and SNC0.95, respectively), a Jahn-Teller (JT) distortion with varying extents takes place, leading to the formation of modified crystal lattice within a perovskite framework. Electrical conductivity, electrochemical performance, chemical compatibility and microstructure of $Sr_{1-s}Nb_{0.1}Co_{0.9}O_{3-\delta}$ as cathodes for solid oxide fuel cells were evaluated. Among SNC1.00, SNC0.98 and SNC0.95, SNC0.95 (P4/mmm symmetry (#123)) which exhibits large JT distortion in conjunction with charge-ordering of cobalt (Co) shows the best oxygen reduction reaction (ORR) activity at low temperature while SNC0.98 (P4mm symmetry (#99)) which displays a local JT distortion shows the poorest performance.

1. Introduction

Solid oxide fuel cell (SOFC) is one of the key technologies enabling clean energy delivery with high conversion efficiency, particularly for power generation from hydrogen, carbon monoxide, methane, coal syngas, and liquid hydrocarbon fuels. Conventional SOFC nonetheless has shortcomings in terms of its high cost and degradation in performance from high temperature operation. To lower the operating temperature, the oxygen reduction reaction (ORR) activity of the SOFC cathode must be improved to maintain high power density.

ABO_3 perovskite-type mixed oxide-ionic and electronic conductors (MIECs) are among excellent cathode candidates for low-temperature SOFCs.[1-8] Up to a reasonable limit, these perovskite oxides can fine-tune their structure (so that their original framework is maintained) to accommodate a mismatch of the equilibrium bond lengths between (and within) the A and B sites, cation and/or anion vacancies, as well as the formation of A- or B-site cation ordering structures.[9] In this context, one strategy has been devised to enhance their oxygen reduction kinetics, e.g. by introducing A-site defects. Several A-site deficient perovskites, namely $La_{0.6}Sr_{0.4-s}C_{o0.2}Fe_{0.8}O_{3-\delta}$,[10] $(Pr_{0.6}Sr_{0.4})_{1-s}Co_{0.2}Fe_{0.8}O_{3-\delta}$,[11] $La_{1-s}Fe_{0.4}Ni_{0.6}O_{3-\delta}$,[12,13] $(Ba_{0.5}Sr_{0.5})_{1-x}Co_{0.8}Fe_{0.2}O_{3-\delta}$,[14] $Ba_{1-x}Co_{0.9-y}Fe_yNb_{0.1}O_{3-\delta}$,[15,16] and $PrBa_{1-s}Co_2O_{5+\delta}$[17] have been investigated as cathode materials for SOFCs. The physical and chemical properties of A-site deficient perovskites are often substantially different from those of the stoichiometric ones. The introduction of A-site defects tends to create additional oxygen vacancies which facilitate oxygen ionic transport and enhance the ORR activity.[18] However, these oxygen vacancies may also interfere with the electron transport, reducing the electronic conductivity of the materials.[19] We found a novel A-site deficient perovskite, $Sr_{0.95}Nb_{0.1}C_{o0.9}O_{3-\delta}$ (SNC0.95) which exhibits substantially improved ORR activity at low temperatures relative to its stoichiometric analogue, $SrNb_{0.1}Co_{0.9}O_{3-\delta}$ (SNC1.00). SNC0.95 features simultaneous enhancement in oxygen vacancy concentration and electrical conductivity,[20] the responsible mechanism of which has not yet been clarified. Here, we show that the $Sr_{1-s}Nb_{0.1}Co_{0.9}O_{3-\delta}$ perovskites (s = 0.02 and 0.05; denoted as SNC0.98 and SNC0.95, respectively) exhibit different crystal structures due to the varying extent of Jahn-Teller (JT) distortions. The effects of crystal structure on the electrical conductivity, electrochemical performance, chemical compatibility and microstructure of the resultant cathode materials are examined. SNC0.95 (P4/mmm crystal structure) shows improved ORR activity at low temperature whereas SNC0.98 (P4mm structure) shows diminished performance. $Sr_{1-s}Nb_{0.1}Co_{0.9}O_{3-\delta}$ perovskites represents a deviation from the general notion of increased concentration of oxygen vacancies leading to enhanced ORR activity.[20-22] Instead, the crystal structure seems to play a more determining role towards its electrochemical performance.

2. Experimental Section

Synthesis of powders: $Sr_{1-s}Nb_{0.1}C_{0.9}O_{3-\delta}$ (s = 0, 0.02, 0.05, 0.1 and 0.2) powders were synthesised using a solid-state reaction. Stoichiometric amounts of $SrCO_3$, Nb_2O_5, and Co_2O_3 (all of analytical grade, from Sinopharm Chemical Reagent Co. Ltd.) were weighed and thoroughly mixed using a planetary mill (Fritsch, Pulverisette 6) and acetone as a solvent at 400 rpm for 1 h. After drying, the powders were calcined at 1200 °C in air for 20 h. The milling and calcination were performed twice to ensure homogeneity and obtain highly pure $Sr_{1-s}Nb_{0.1}Co_{0.9}O_{3-\delta}$ phase for characterisation and testing.

Fabrication of the symmetrical cells: Symmetrical cells with an electrode|$Sm_{0.2}Ce_{0.8}O_{1.9}$(SDC)|electrode configuration were fabricated for electrochemical impedance spectroscopy (EIS) measurements. Dense SDC disks (0.8 mm thickness, 12.5 mm diameter) were prepared by dry pressing followed by sintering at 1400 °C for 5 h. The cathode powders were firstly dispersed in a pre-mixed solution of glycerol, ethylene glycol, and isopropyl alcohol. A colloidal suspension was obtained from this mixture by a planetary milling (Fritsch, Pulverisette 6) at 400 rpm for 0.5 h. The suspension was coated by spray deposition onto both sides of the dense SDC disk and calcined at 1000 °C for 2 h in air to obtain porous electrodes. For current collection, a thin layer of silver paste was painted onto the electrode surface and dried at 100 °C.

Characterisation: The crystal structures of the powders were determined by room temperature powder X-ray diffraction (XRD, D8 Advance, Bruker, Germany) with filtered Cu-Kα radiation (40 kV and 40 mA) using a receiving slit of approximately 0.2 mm. The experimental diffraction patterns were collected by scanning between 2θ=10–90° with a step size of 0.05°. The α2 component of the filtered radiation was stripped-off. Structure refinements of the XRD patterns were carried out using DIFFRACplus Topas 4.2 software.[23] During the refinements, general parameters such as the scale factor, background parameters, and the zero point of the counter were optimised. Le Bail refinement was used initially to determine the space group and to approximate the lattice parameters of the SNC, SNC0.98 and SNC0.95. Rietveld refinement was then performed to determine the general position of the atoms. The oxygen occupancy is fixed to 1. It is considered futile to determine oxygen content (since oxygen has relatively low molecular weight) in the presence of heavy element using XRD pattern.

The chemical compatibility between the cathode and the SDC electrolyte materials was examined. $Sr_{1-s}Nb_{0.1}Co_{0.9}O_{3-\delta}$-SDC powders mixtures (1:1 weight ratio) were calcined at 1000 °C for 2 h in air atmosphere. The phase composition of the mixture after calcinations was analysed by powder X-ray diffraction (XRD, D8 Advance, Bruker, Germany) at room temperature.

The oxygen non-stoichiometry and the valence states of cobalt at room temperature were determined by iodometric titration. In brief, approximately 0.1 g of powder was dissolved in a 6 mol L^{-1} HCl solution in a nitrogen atmosphere to prevent the oxidation of I^- ions (from KI) by air, followed by titration with a standard thiosulfate ($S_2O_3^{2-}$) solution. The oxygen non-stoichiometry and the valence states of cobalt at high temperatures were measured by thermogravimetric analysis (TGA, Model STA 449 F3, NETZSCH) in a synthetic air atmosphere from room temperature to 1000 °C. The heating and cooling rates were 10 °C min^{-1}.

The cathode powders were packed into rectangular bars with dimensions of 2 mm × 5 mm × 20 mm and sintered at 1200 °C for 5 h in air for electrical conductivity testing. All bars used for measurements had densities of > 93% of their theoretical values. Electrical conductivity was measured using a four-probe DC technique with silver coating layer as electrodes. The current and voltage were measured using a Keithley 2420 source meter; the data was collected at a 25 °C interval between 450 and 800 °C in an air atmosphere.

Raman spectra were recorded in a backscattering mode at room temperature using a LABRAM inVia micro-Raman system equipped with an optical microscope containing a 50× objective lens. The radiation source was a He-Ne laser (λ = 514 nm) operated at 1% power, which was focused on a 5 µm spot at 40 mW. Before measurement, the micro-Raman system was calibrated using the 520 cm^{-1} peak of polycrystalline Si.

Transmission electron microscopy (TEM) was conducted at 220 kV with a Philips T30F field emission instrument equipped with a 2k-CCD camera and JEOL 2100F TEM equipped with a Schottky field-emission gun (FEG), with Cs =1.0 mm operated at 200 kV. Double tilting was applied to find the right zone axis as required. The morphologies of the cathode and cathode/electrolyte interface were obtained using an environmental scanning electron microscope (ESEM, QUANTA-2000). The selected area electron diffraction (SAED) simulation patterns based on the XRD refinements results were obtained using the CrystalMaker (2.5.1) and SingleCrystal (2.0.1) software.[24]

Electrochemical measurements: EIS of the cathode was obtained by AC impedance measurements using an electrochemical workstation composed of a Solartron 1260A frequency response analyser and a Solartron 1287 potentiostat. The symmetrical cells were tested between 450–750 °C in an ambient air atmosphere. The applied frequency range was from 0.01 Hz to 100 kHz, and the signal amplitude was 10 mV. The measurement was performed under an open cell voltage (OCV) condition. Electrode polarisation resistance data were analysed with Z-plot 3.0c software.

3. Results and discussion

Structure characterisation

Fig 1a shows the XRD patterns of $Sr_{1-s}Nb_{0.1}Co_{0.9}O_{3-\delta}$ (s = 0, 0.02 and 0.05) powders calcined at 1200 °C. SNC1.00, SNC0.98 and SNC0.95 contain a single phase. A second phase, CoO, however appears on the XRD patterns when A-site deficiency was made in excess of 5% (Supporting Information, Fig S1).

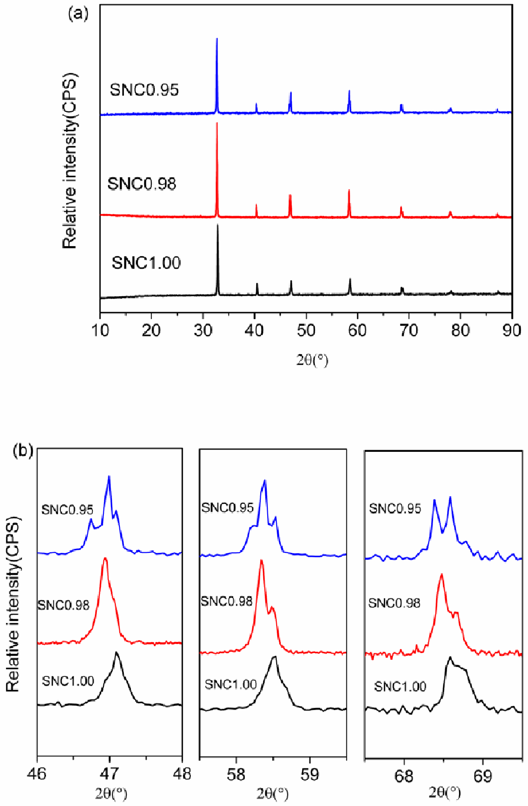

Fig.1 (a) X-ray diffraction patterns of SNC1.00, SNC0.98 and SNC0.95 powders calcined at 1200 °C; (b) Magnified XRD patterns around 2θ= 47°, 48.5° and 68.5°.

To avoid complications from the second phase, we limit our scope to SNC1.00, SNC0.98, and SNC0.95. SNC0.95 has a tetragonal structure, the symmetry of which can be described by the P4/mmm space group (#123). This is implied by the line splitting of peaks at approximately 47°, 58.5° and 68.5°, which was not observed in SNC1.00 and SNC0.98 (Fig 1b). Raman spectroscopy was used to probe the symmetry of the crystal structure of SNC1.00, SNC0.98, and SNC0.95 (Fig 2). No vibrational modes were observed for SNC1.00, indicating high symmetry, i.e., a Pm-3m cubic symmetry.[25] Six modes were identified for SNC0.95, in agreement with the symmetry of the P4/mmm space group.[26] We further confirmed the cubic and tetragonal lattice for SNC1.00 and SNC0.95, respectively, by high resolution (HR)TEM and selected area electron diffraction (SAED) (Fig 3). The HRTEM image and the corresponding SAED pattern of SNC1.00 are indeed characteristic of the primitive cubic perovskite symmetry best described by Pm-3m space group (#221) with $a = a_p = 3.9$ Å. For SNC0.95, the reconstruction of the reciprocal space from the SAED pattern revealed a tetragonal cell with $a \approx a_p$ and $c \approx 2a_p$, compatible with the P4/mmm space group. The doubled cell parameter value with respect to the primitive perovskite cell is clearly indicated on the HRTEM image and the corresponding SAED pattern.

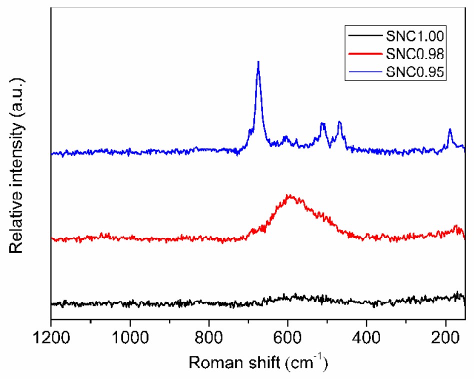

Fig.2 Raman spectra of SNC1.00, SNC0.98 and SNC0.95.

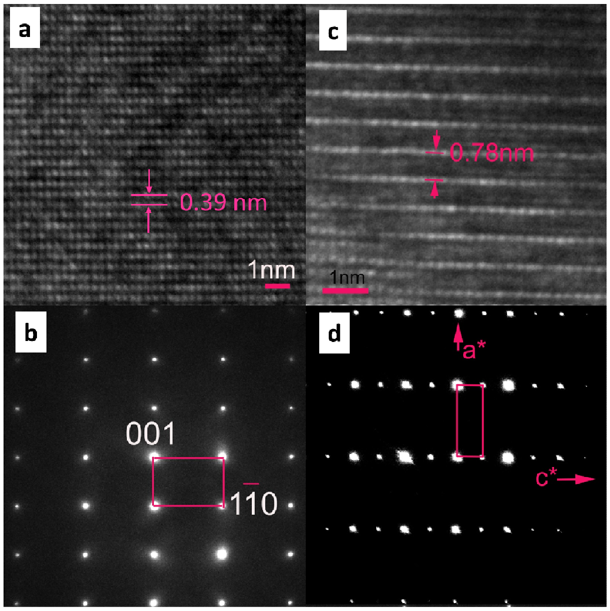

Fig.3 HRTEM images of (a) SNC1.00 and (c) SNC0.95; SAED images of (b) SNC1.00 and (d) SNC0.95.[20]

The structure of SNC0.98 cannot be directly identified by XRD. SNC1.00 and SNC0.98 powders showed similar XRD patterns but distinct Raman vibrational modes (Fig 2). The broad band at ~590 cm^{-1} in the spectrum of SNC0.98 was indicative of degradation of ideal cubic symmetry; most likely attributed to a local JT distortion.[27] The JT distortion may lead to a tetragonal distortion in the CoO_6 octahedra.[27] Slight decrease in the symmetry of the diffraction peaks (Fig 1b) implies the likelihood of a P4mm symmetry, as is the case of $BaTiO_3$ perovskite.[28] We refined the structure of SNC0.98 using model based on centrosymmetric Pm-3m, noncentrosymmetric P4mm and centrosymmetric P4/mmm space group. P4mm space group (#99) model gave the lowest residuals among the three models (Table S1). Low electrical conductivity SNC0.98 seems to somewhat correlate with the noncentrosymmetric structure as suggested by the following conductivity results. The phase stability was then probed using high-temperature (HT)-XRD (Fig 4). The splitting of the peaks at 47°, 58.5° and 68° is retained up to 800 °C; ruling out the possible phase transformation during SOFC operation.

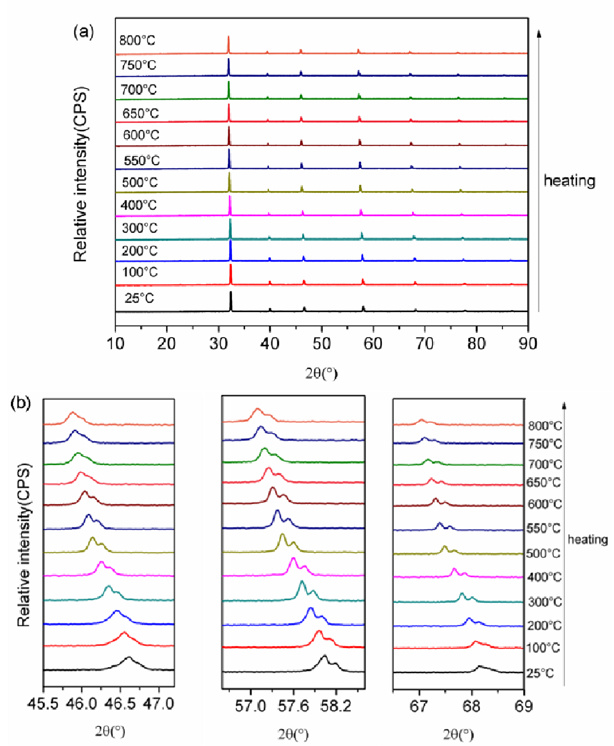

Fig.4 (a) HT-XRD patterns of the SNC0.98 powder between room temperature to 800 °C. (b) Magnified XRD patterns around 2θ= 47°, 48.5° and 68.5°.

HRTEM was used to examine the crystal structure of SNC0.98. Fig 5 indicates identical lattice structure between SNC0.98 and SNC1.00. It is not possible to confidently distinguish P4mm from Pm-3m symmetry using HRTEM and SAED results, considering the relatively weak tetragonal distortion as reflected by the ratio of c/a of only 1.003 (for P4mm symmetry).[29] This is particularly apparent upon comparing the Fast Fourier Transform (FFT) images with the simulated electron diffraction spots (Fig 5d-f to Fig 5g-i).

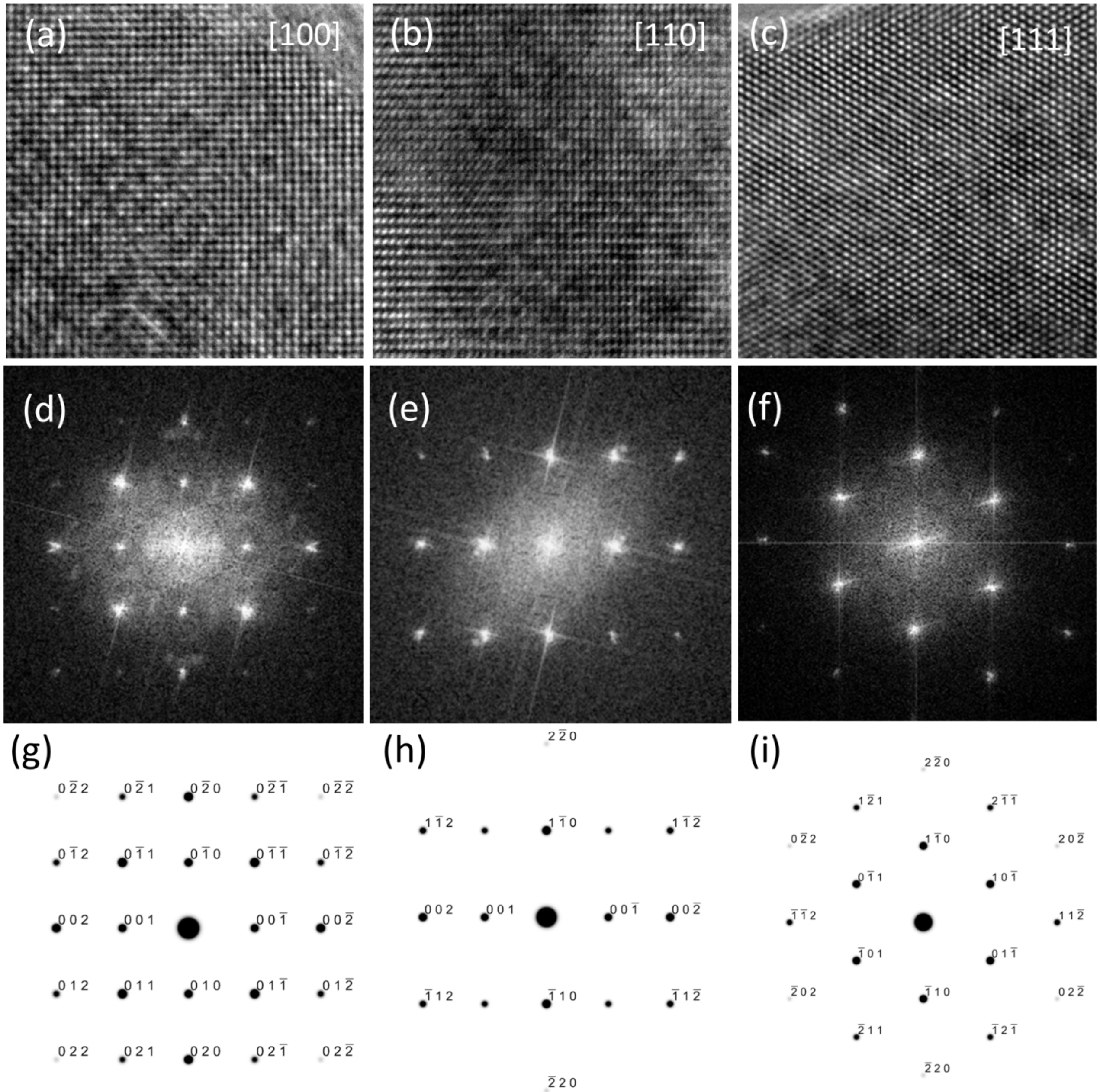

Fig.5 HRTEM images (a-c); Fast Fourier Transform (FFT) images (d-f) of [100], [110], [111] zone axes for SNC0.98 and the simulated diffraction patterns of (g) [100], (h) [110], (i) [111] zone axes for SNC0.98 in P4mm space group with lattice parameters listed in Table S2.

Lattice parameters of SNC1.00, SNC0.98 and SNC0.95 were obtained by Rietveld refinement (Fig S2 and Table S2). Introduction of A-site defects in $Sr_{1-s}Nb_{0.1}Co_{0.9}O_{3-\delta}$ perovskites led to lattice expansion for both SNC0.98 and SNC0.95. The (Co,Nb)-O bond lengths and O-(Co,Nb)-O angles in SNC1.00, SNC0.98 and SNC0.95 are listed in Table 1. The crystal structure transitions from Pm-3m to P4mm and P4/mmm are depicted schematically in Fig 6. The P4mm structure exemplified a tetragonal distortion of the cubic perovskite, resulting in a difference of (Co,Nb)-O1 and (Co,Nb)-O1* bond lengths. As a result, (Co,Nb)-O1* bond can be visualised to be excluded from an originally symmetric $(Co,Nb)O_6$ octahedron (imagine taking out O1* from one of the opposing apex) so that the repeating unit becomes a distorted $(Co,Nb)O_5$ square pyramid which shares corner with other units (in the same layer). For 0.05 A-site deficiency case, although each (Co,Nb)-O1* and (Co,Nb)-O1 bond shows similar bond length value (1.8810 Å and 2.0075 Å, respectively), they are distributed periodically in two different $(Co,Nb)O_6$ octahedron, forming an overall framework described by P4/mmm symmetry. Perhaps, the doubling of the lattice in SNC0.95 originates from long-range ordering of oxygen vacancies along the c axis, which brings about the charge-ordering between Co^{4+} and Co^{3+} cations. Charge ordering is a phase transition observed mostly in strongly correlated materials such as transition metal oxides.[30-32] Strong interaction between electrons in these materials lead to localised charges on different sites and thus, a disproportionation and an ordered superlattice.[33] Here, two types of $(Co,Nb)O_6$ octahedron exist within the P4/mmm framework; the elongated one e.g. $(Co,Nb)1O_6$ octahedron containing two stacked (Co,Nb)1–O2 bonds of 2.0075 Å length each (as the 4-fold axis) while the shortened one e.g. $(Co,Nb)2O_6$ octahedron containing two stacked (Co,Nb)2–O2 bonds of 1.8810 Å length each (also as 4-fold axis). In both cases, the square centre of the octahedron is symmetrical as reflected by 4 equivalent bond length of (Co,Nb)1-O1 and (Co,Nb)2-O3 (e.g. 1.9348 Å). Since the average valence for Co is 3.2+ (Table 2), the charge-ordering hypothesis signifies an average oxidation state of Co^{3+} at $(Co,Nb)1O_6$ sites and $Co^{3.4+}$ at $(Co,Nb)2O_6$ sites, assuming a full charge disproportionation. A similar structure was also noticed earlier in a $SrSb_{0.1}Co_{0.9}O_{3-\delta}$ perovskite.[34]

Table 1. (Co,Nb)-O bond lengths and angles of O-(Co,Nb)-O for SNC1.00, SNC0.98 (P4mm symetry) and SNC0.95.

SNC1.00			
(Co,Nb)-O×6	1.936(3)	O-(Co,Nb)-O	180º
SNC0.98			
(Co,Nb)-O1	1.837(0)	O1-(Co,Nb)-O1*	180º
(Co,Nb)-O1*	2.055(2)		
(Co,Nb)O2×4	1.986(9)	O2-(Co,Nb)-O2	154.92º
SNC0.95			
(Co,Nb)1-O2×2	2.007(5)	O2-(Co,Nb)1-O2	180º
(Co,Nb)2-O2×2	1.881(0)	O2-(Co,Nb)2-O2	180º
(Co,Nb)1-O1×4	1.934(8)	O1-(Co,Nb)1-O1	180º
(Co,Nb)2-O3×4	1.934(8)	O3-(Co,Nb)2-O3	180º

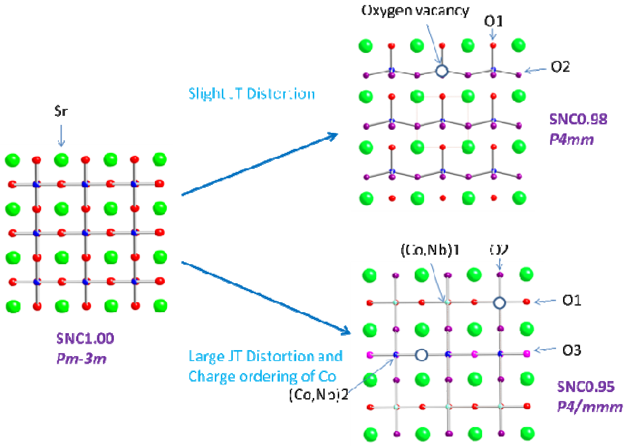

Fig.6 Schematic of the structure transition from Pm-3m (SNC1.00) to P4mm (SNC0.98) and P4/mmm (SNC0.95).

Table 2. Valence states of cobalt and oxygen non-stoichiometry (δ) of SNC1.00, SNC0.98 and SNC0.95 at room temperature.

Sample	δ	Valence states of cobalt
SNC1.00	0.24	3.3
SNC0.98	0.38	3.0
SNC0.95	0.35	3.2

We speculate that the JT distortion offsets the increased energy of the perovskite system induced by a 2% A-site deficiency. Nonetheless, increasing the deficiency to 5% cannot be compensated by slight (local) JT distortion. SNC0.95 shows substantial JT distortion reflected by $(Co,Nb)1O_6$ with elongated axial bond and $(Co,Nb)2O_6$ with shortened axial bond. Both distortions will lower the energy for a system with one eg electron (for $(Co,Nb)1O_6$ the z^2 orbital is lowered and x^2-y^2 orbital for $(Co,Nb)2O_6$ just the opposite direction, and in both cases the lowest eg orbital is singly occupied). Therefore, besides the JT distortion, the elastic energy would be further minimised by such an ordering with shorter and longer bond lengths.[22,35,36]

Within the perovskite, each O^{2-} is surrounded by 4 A-site cations and 2 B-site cations. The formation of one A-site vacancy necessitates a change in the local coordination number (CN) from 6 to 5 for O^{2-}. Given that no O^{2-} ions with CN = 5 is possible,[37] the distortions of the oxygen sublattice somehow need to be compensated by modifying the perovskite structure. $La_{1/3}NbO_3$, for example can accommodate a large A-site deficiency since Nb-O has a high degree of covalence to stabilise the Nb–O network.[38] However, for transition metal cations which can easily change their oxidation states (such as Co), a stable CoO_6 octahedron is difficult to obtain (upon subjected to A-site deficient). Konysheva et al. provides simple prediction criteria to estimate the extent of the A-site deficiency in perovskites based on the average <B-O> bond energy and metal (A,B)–oxygen bond energy (<ABE>) within the perovskite lattice.[38] In our case, Co is partially replaced with 10% Nb to enhance the stability of the B-site octahedral network. The <B-O> bond energy for $A(Nb^{5+}{}_{0.1}Co^{3+}{}_{0.9})O_{3-\delta}$ perovskites is -207 kJ mol^{-1}, suggesting the maximum defect concentration of 0.06 (Supporting information, Figure S3). Nonetheless, when the <ABE> value is applied as the prediction descriptor (the properties of the particular A-site cations are involved in this prediction), the A-site deficiency is unattainable in $Sr_{1-s}Nb_{0.1}Co_{0.9}O_{3-\delta}$; given the more positive value of <ABE> in SNC0.95 (-287 kJ $mol^{-1,}$ supporting information, Fig S4). The obtainment of 5% A-site deficient (SNC0.95) perovskite phase here highlights the fact that the stability of B-site octahedron provides a more dominant role.

Oxygen nonstoichiometry and electrical conductivity

In general, additional oxygen vacancies may negatively impact the electronic transport; normally evidenced by a decrease in the electrical conductivities (of some A-site deficient perovskites).[10,14,19,39] Fig 7 depicts the oxygen vacancy concentrations of SNC1.00, SNC0.98, and SNC0.95 between 450-800 °C. Additional oxygen vacancies actually formed with the increase in A-site defects as described by Eqn (1).

$$Sr_{Sr}^{\times} + O_{O}^{\times} \rightarrow V_{Sr}'' + V_{O}^{\cdot\cdot} + SrO \qquad (1).$$

SNC0.98 has the largest oxygen vacancy concentration in the temperature range studied. Fig 8 displays the electrical conductivities of SNC1.00, SNC0.98 and SNC0.95 between 450-800 °C. Whilst reduced electrical conductivity of SNC0.98 (relative to SNC1.00) is consistent with its higher concentration of oxygen vacancies, SNC0.95 deviates from this trend. Despite its larger concentration of oxygen vacancies, in fact, the electrical conductivity of SNC0.95 exhibits values between 276-117 S cm^{-1},[20] higher than those of 265-83 S cm^{-1} for SNC1.00. This synergistic effect is perhaps related to its intrinsic structure with P4/mmm symmetry. It is very likely that the charge ordering of Co favours rapid electron transport in SNC0.95.

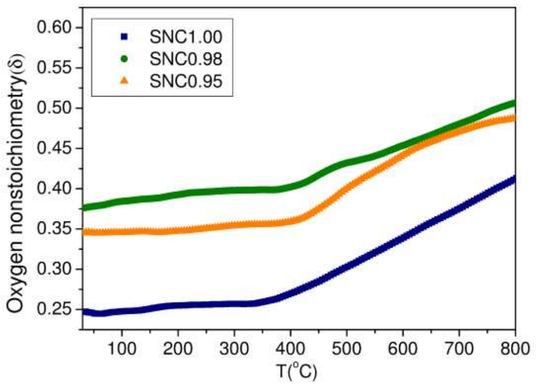

Fig.7 Oxygen vacancy concentrations of SNC1.00, SNC0.98 and SNC0.95 between 25-800 °C.

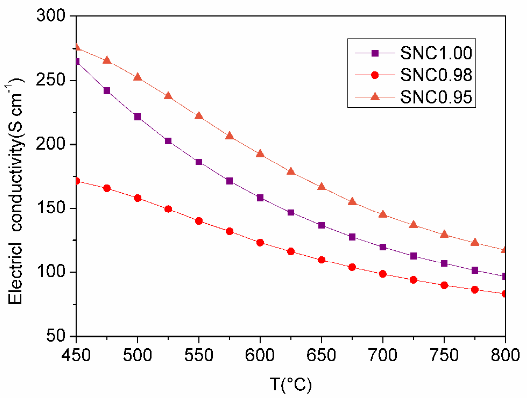

Fig.8 Electrical conductivities of SNC1.00, SNC0.98 and SNC0.95 [20] between 450-800 °C.

Chemical and thermal compatibility

Several A-site deficient perovskites, such as (La,Sr)MnO$_3$ (LSM) and (La,Sr)FeO$_3$ (LSF) displayed good chemical compatibility with YSZ electrolytes; associated with the absence of highly resistive SrZrO$_3$ and La$_2$Zr$_2$O$_7$ phases at the electrode-electrolyte interface.[40.41] However, in a previous study, we reported that introducing A-site deficiency led to detrimental phase reactions between (A-site-deficient) Ba$_{0.5}$Sr$_{0.5}$Co$_{0.8}$Fe$_{0.2}$O$_{3-\delta}$ (BSCF) perovskites and Sm$_{0.2}$Ce$_{0.8}$O$_{1.9}$ (SDC) at 1000 °C during which inert phase(s) formed which inhibited the ORR.[14] Fig 9 shows the XRD patterns of Sr$_{1-s}$Nb$_{0.1}$Co$_{0.9}$O$_{3-\delta}$-SDC mixed powders (1:1 weight ratio) calcined at 1000 °C. No other diffraction peaks apart from those characteristics of single-phase Sr$_{1-s}$Nb$_{0.1}$Co$_{0.9}$O$_{3-\delta}$ and SDC were perceived. This indicates good chemical compatibility of Sr$_{1-s}$Nb$_{0.1}$Co$_{0.9}$O$_{3-\delta}$ perovskites against SDC electrolytes.

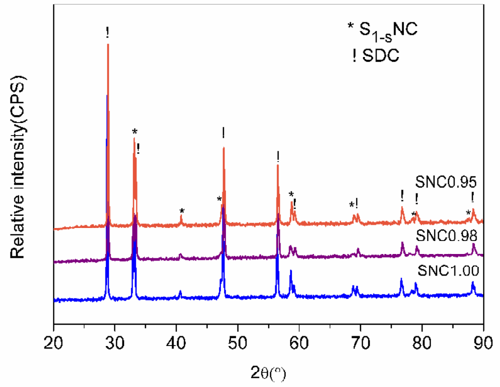

Fig.9 XRD patterns of SNC1.00-SDC, SNC0.98-SDC and SNC0.95-SDC [20] mixed powders (1:1 weight ratio) calcined at 1000 °C for 2h.

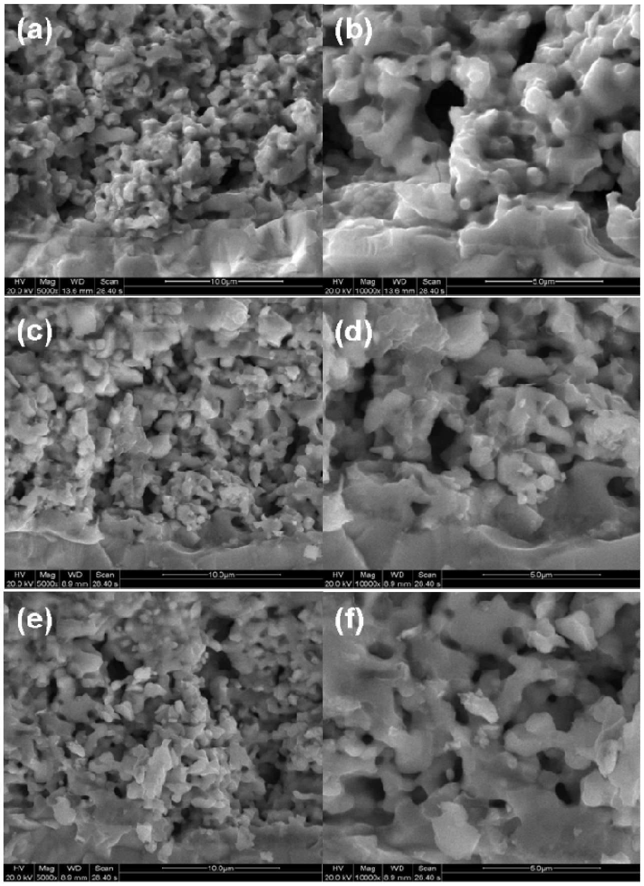

Fig.10 SEM images of (a, b) SNC1.00, (c, d) SNC0.98 and (e, f) SNC0.95 cathodes calcined at 1000 °C for 2 h in air. The scale bars are 10 µm for (a), (c), (e) and 5 µm for (b), (d), (f).

The microstructures of the Sr$_{1-s}$Nb$_{0.1}$Co$_{0.9}$O$_{3-\delta}$ cathodes are shown in Fig 10. Firm attachment between the cathode and electrolyte suggests good thermal compatibility between Sr$_{1-s}$Nb$_{0.1}$Co$_{0.9}$O$_{3-\delta}$ perovskites and SDC. The grain sizes and pore structures look very similar for the three cathodes, which dismisses microstructural effects on the electrochemical performance.

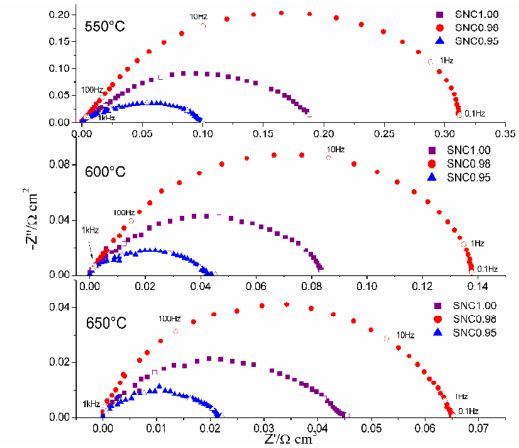

Fig.11 Electrochemical impedance spectra of SNC1.00, SNC0.98 and SNC0.95 cathodes between 550-650 °C.

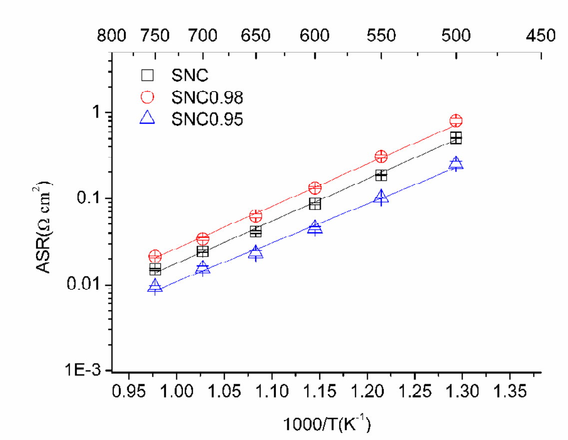

Fig.12 Temperature dependent ASRs of $Sr_{1-s}Nb_{0.1}Co_{0.9}O_{3-\delta}$ cathodes tested between 500 and 750 °C. Error bars represent standard deviations of three independent measurements.

Oxygen reduction reaction activity

Fig 11 shows typical impedance spectra for the $Sr_{1-s}Nb_{0.1}Co_{0.9}O_{3-\delta}$ cathodes between 550-650 °C. The difference between the intercepts of the impedance arc on the real axis is the interfacial resistance of the cathode, denoted as the area specific resistance (ASR). The ASRs were measured to be 0.19, 0.31 and 0.10 Ω cm^2 for SNC1.00, SNC0.98, and SNC0.95 at 550 °C, respectively. Figure 12 shows the thermal evolution of the ASR values of the three cathodes prepared under identical conditions. Since ASRs measured on porous electrodes are susceptible to changes in morphology of the electrodes, each data point was taken from three measurements on three different specimens (with same composition). The microstructure and thickness of all electrodes are very similar to each other (Figure S5). The SNC0.95 cathode showed lower ASR values relative to SNC1.00, whereas the SNC0.98 cathode displays lower ORR activity with respect to SNC1.00. With negligible effects from microstructure and reaction between cathode and electrolyte, the observed trend closely represents the intrinsic properties of $Sr_{1-s}Nb_{0.1}Co_{0.9}O_{3-\delta}$. Within the context of correlating structure-electrochemical properties specific to $Sr_{1-s}Nb_{0.1}Co_{0.9}O_{3-\delta}$, a (slight) local JT distortion seems to contribute negatively towards the electron transport and the ORR activity.

4. Conclusions

In summary, we demonstrated the effect of crystal structure on the ORR activity of SNC0.98 and SNC0.95 cathodes. Relative to SNC1.00 (Pm-3m symmetry), SNC0.95 (P4/mmm symmetry) which displays a large JT distortion in combination with charge-ordering of Co, shows improved ORR activity at low temperature, whereas SNC0.98 (P4mm symmetry) which exhibits slight (local) JT distortion, shows lower performance.

Acknowledgements

This work was supported by the China National Funds to Distinguished Young Scientists under No. 51025209, the Outstanding Young Scholar Grant at Jiangsu Province under No. 2008023, the Fok Ying Tung Education Grant under contract No. 111073, the Program for New Century Excellent Talents in Chinese Ministry of Education and the National Basic Research Program of China under contract No. 2007CB209704, and Australian Research Council (ARC). YL and FC were supported by the HeteroFoaM Center, an Energy Frontier Research Center funded by Office of Science, U.S. Department of Energy under Award Number DE-SC0001061. Electron microscopy research was partially carried out at the Center for Functional Nanomaterials, Brookhaven National Laboratory, which is supported by the U.S. Department of Energy, Office of Basic Energy Sciences, under contract no. DE-AC02-98CH10886. XS thanks the China Scholarship Council and Brookhaven National Laboratory for the financial support for his exchange program.

Notes and references

[a] *State Key Laboratory of Materials-Oriented Chemical Engineering*
College of Chemistry & Chemical Engineering
Nanjing Tech University
No. 5 Xin Mofan Road, Nanjing 210009 (P.R. China)
[b] *Department of Mechanical Engineering*
University of South Carolina
Columbia, South Carolina 29208, (USA)
[c] *Center for Functional Nanomaterials, Brookhaven National Laboratory*
Upton, NY 11973, (USA)
[d] *National Laboratory of Solid State Microstructures*
Department of Materials Science and Engineering
Nanjing University,
Nanjing 210093, (P.R. China)
[e] *Department of Chemistry*
University of Waterloo
200 University Avenue West, Waterloo, Ontario, N2L 3G1, (Canada)
[f] *School of Chemical Engineering*
The University of Queensland
Brisbane, Queensland 4072 (Australia)
E-mail: wei.zhou@uq.edu.au
[g] *State Key Laboratory of Materials-Oriented Chemical Engineering*
College of Energy
Nanjing Tech University
No. 5 Xin Mofan Road, Nanjing 210009 (P.R. China)
Fax: (+86) 25-83172256
E-mail: shaozp@njtech.edu.cn

† Electronic Supplementary Information (ESI) available: [details of any supplementary information available should be included here]. See DOI: 10.1039/b000000x/

1 H. U. Anderson, *Solid State Ionics*, 1992, **52**, 33.
2 B. C. H, Steel and A. Heinzel, *Nature*, 2001, **414**, 345.
3 Z. P. Shao and S. M. Haile, *Nature*, 2004, **431**, 170.

4 Z. P. Shao, W. S. Yang, Y, Cong, H. Dong, J. H. Dong and G. Q. Xiong, *J. Membr. Sci*., 2000, **172**, 177
5 Q. M. Li, X. F. Zhu, Y. F. He and W. S. Yang, *Catal Today*, 2000, **149**, 185.
6 J. H. Kim, M. Cassidy, J. T. S. Irvine and J. Bae, *Chem Mater*., 2010, **22**, 883.
7 T. Hibino, A. Hashimoto, T. Inoue, J. Tokuno, S. Yoshida and M. Sano, *Science*, 2000, **288**, 2031.
8 T. Z. Sholklapper, H. Kurokawa, C. P. Jacobson, S, J. Visco and L. C. De Jonghe, *Nano Lett*., 2007, **7**, 2136.
9 J. B. Goodenough, *Rep. Prog. Phys*., 2004, **67**, 1915.
10 G. C. Kostogloudis and C. Ftikos, *Solid State Ionics*, 1999, **126**, 143.
11 K. K. Hansen, *J. Electrochem. Soc*., 2009, **156**, B1257.
12 E. Konysheva and J. T. S.Irvine, *J. Mater Chem*., 2008, **18**, 5147.
13 J. Knudsen, P. B. Friehling and N. Bonanos, *Solid State Ionics*, 2005, **176**, 1563.
14 W. Zhou, R. Ran, Z. P. Shao, W. Q. Jin and N. P. Xu, *J. Power Sources*, 2008, **182**, 24.
15 Z. B. Yang, C. H. Yang, C. Jin, M. F. Han and F. L. Chen, *Electrochem Commun*, 2011, **13**, 882.
16 Z. Liu, L. Z. Cheng and M. F. Han, *J. Power Sources*, 2011, **196**, 868.
17 Z. B. Yang, M. F. Han, P. Y. Zhu, F. Zhao and F. L. Chen, *Int. J. Hydrogen Energy*, 2011, **36**, 9162.
18 K. K. Hansen and K. Vels Hansen, *Solid State Ionics*, 2007, **178**, 1379.
19 A. Mineshige, J. Izutsu, M. Nakamura, K. Nigaki, J. Abe, M. Kobune, S. Fujii and T. Yazawa, *Solid State Ionics*, 2005, **176**, 1145.
20 Y. L. Zhu, Z. G. Chen, W. Zhou, S. S. Jiang, J. Zou and Z. P. Shao, *ChemSusChem*, 2013, **6**, 2294.
21 W. Zhou, Z. P. Shao, R. Ran, W. Q. Jin and N. P. Xu, *Chem. Commun*., 2008, 5791.
22 W. Zhou, J. Sunraso, Z. G. Chen, L. Ge, J. Motuzas, J. Zou, G. X. Wang, A. Julbe and Z. H. Zhu, *Energy Environ. Sci*., 2011, **4**, 872.
23 DIFFRACPlus TOPAS 4.2 software, Bruker-AXS GmbH, Karlsruhe, Germany, 2008.
24 CrystalMaker and SingleCrystal software, CrystalMaker Software Ltd., Oxford, England, 2014.
25 E. Granado, N. O. Moreno, A. García, J. A. Sanjurjo, C. Rettori, I. Torriani, S. B. Oseroff, J. J. Neumeier, K. J. McClellan, S. W. Cheong and T. Tokura, *Phys. Rew. B*, 1998, **58**, 11435.
26 R. Lownders, M. Deluca, F. Azough and R. Freer, *J. Appl. Phys*. 2013, **113**, 044115.
27 S. Gangopadhayay, T. Inerbaev, A. E. Masunov, D. Altilio and N. Orlovskaya, *ACS Appl. Mater. Interfaces*, 2009, **7**, 1512.
28 B. D. Begg, K. S. Finnie and E. R. Vance, *J. Am. Ceram. Soc*, 1996, **79**, 2666.
29 M. Otonicar, S. D. Skapin, B. Jancar, R. Ubic and D. Suvorov, *J. Am. Ceram. Soc*, 2010, **93**,4168.
30 Y. Tokura and N. Nagaosa, *Science*, 2000, **288**, 462.
31 G. Kotliar and D. Vollhardt, *Physics Today*, 2004, **57**, 53.
32 E. Dagotto, *Science*, 2005, **309**, 257.
33 T. Goto and B. Lüthi, *Advances in Physics*, 2003, **52**, 67.
34 A. Aguadero, C. de la Calle, J. A. Alonso, M. J. Escudero, M. T. Fernández-Díaz and L. Daza, *Chem. Mater*., 2007, **19**, 6437.
35 W. Zhou, J. Sunarso, J. Motuzas, F. L. Liang, Z. G. Chen, L. Ge, S. M. Liu, A. Julbe and Z. H. Zhu, *Chem. Mater*., 2011, **23**, 1618.
36 Y. Li, J. G. Cheng, J. Song, J. A. Alonso, M. T. Fernández-Díaz and J. B. Goodenough, *Chem. Mater*., 2012, **24**, 4114.
37 R. D. Shannon and C. T. Rewitt, *Acta Cryst. B*, 1969, **25**, 925.
38 E. Konysheva, X. X. Xu and J. T. S. Irvine, *Adv. Mater*., 2012, **24**, 528.
39 X. Li, H. L. Zhao, X. O. Zhou, N. S.Xu, Z. X. Xie and N. Chen, *Int. J. Hydrogen Energy*, 2010, **35**, 7931.
40 D. L. Meixner and R. A. Cutler, *Solid State Ionics*, 2002, **146**, 273.
41 U. F. Vogt, P. Holtappels, J. Sfeir, J. Richter, S. Duval, D. Wiedenmann and A. Zuttel, *Fuel Cells*, 2009, **9**, 899.